INTERNATIONAL JOURNAL FOR NUMERICAL METHODS IN FLUIDS, VOL. 20, 559–572 (1995)

MELTING OF A PCM INSIDE A VERTICAL CYLINDRICAL CAPSULE

YONG KE WU

Département des Sciences Appliquées, Université du Québec à Chicoutimi, Chicoutimi, Québec, G7H 2B1, Canada,

MARCEL LACROIX

Département de Génie Mécanique, Université de Sherbrooke, Sherbrooke, Québec, J1K 2R1, Canada

SUMMARY

A numerical study of natural convection melting of a phase change material within an isothermal vertical cylinder was conducted. The governing conservation equations are formulated in terms of a stream function, vorticity and temperature. Body-fitted co-ordinates are employed for tracking the irregular shape of the timewise changing solid–liquid phase front. Results show that the convective flow patterns and time evolution of the phase front, resulting from simultaneous bottom, side and top heating, are far more complicated than those for the melting from a single isothermal boundary. The heat transfer rate at the top surface is found to decrease monotonically to zero as convection is fully developed in the melt. The highest heat transfer rates are observed at the bottom surface where Bénard convective cells develop. Due to the convective motion of the melt along the vertical heated wall, the onset of Bénard convection occurs at a much earlier time than that for the case of melting within a cylinder heated from below.

KEY WORDS: melting; natural convection; body-fitted co-ordinates

INTRODUCTION

Over the last decade, solid–liquid phase change in cylindrical enclosures with natural convection in the liquid phase has received increasing research attention due to its applications to latent heat of fusion energy storage systems. During the period of storage, a working fluid flows around the cylindrical capsule containing the Phase Change Material (PCM) and heat is transferred to the PCM. Soon the PCM reaches its fusion temperature and melting is triggered. The liquid produced during the melting process is non-uniform in temperature and so natural convection motions occur. In many cases, the buoyancy driven motions become strong enough to rule the melting process. During the period of heat extraction, the PCM releases heat back to the working fluid by solidifying.

Several authors have tackled the problem of natural convection dominated melting inside a horizontal tube[1–6] and inside a horizontal cylindrical annulus.[7] The melting process was investigated analytically and experimentally for a wide range of thermal conditions and melting scenarios. Relatively fewer studies are devoted, however, to the problem of melting inside vertical cylindrical enclosures. Sparrow *et al.*[8] carried out experiments on the melting of a PCM in a vertical isothermal tube. The upper surface of the PCM was bounded by an insulated air space. Numerical solutions based on a pure conduction model were also performed for comparison

CCC 0271–2091/95/060559–14

Received 7 February 1994
Revised 2 November 1994

purposes. It was found that the experimentally determined values of the energy transfer associated with the melting process were about 50 per cent higher than those predicted by the conduction model. These results provided conclusive evidence that natural convection heat transfer in the liquid controls the rate of melting and the shape of the solid–liquid interface.

More recently, Prud'homme *et al.*[9] presented a numerical study of melting within a vertical cylindrical enclosure heated at a constant temperature from below. Results showed that the shape and the motion of the solid–liquid interface are strongly perturbed by the time-dependent multicellular convective flow patterns which develop at the bottom of the enclosure. The Nusselt number at the bottom wall also exhibited strong local variations which are closely related to the evolution of the cell patterns.

The purpose of the present study is to investigate numerically natural convection dominated melting of a PCM within a vertical isothermal capsule. This is a challenging problem as melting is triggered from simultaneous bottom, side and top heating. The objective is not to perform detailed parametric calculations but rather to analyse the timewise complex flow patterns and thermal behaviour of the melt. In the next section, the physical model and the numerical procedure are presented. Results are then reported for the time evolution of the flow patterns and isotherm maps and for the temporal variation of the average Nusselt numbers and molten volume fractions. The effect of the Rayleigh number on the melting process is also examined.

PHYSICAL MODEL AND BASIC EQUATIONS

The PCM is contained in a cylindrical enclosure of height H and radius r_0 (Figure 1(a)). The PCM is assumed to be initially at its fusion temperature T_f, eliminating the need for solution of the energy equation in the solid. At time $t = 0$, the surface temperature of the entire capsule is raised impulsively to a prescribed temperature above the fusion point, $T_w > T_f$. As a result, inward melting is triggered. It is assumed in the analysis that the thermophysical properties of the PCM are independent of temperature. The fluid is Newtonian, incompressible, and the Boussinesq approximation is valid, i.e. liquid density variations arise only in the buoyancy source term, but are otherwise neglected. Fluid motion and heat transfer in the melt are laminar and symmetrical about the vertical centreline. Volumes changes and viscous dissipation are neglected.

Under the foregoing assumptions, the partial differential equations governing the transport of mass, momentum and energy are

continuity equation

$$\frac{\partial(ru)}{\partial r} + \frac{\partial(rv)}{\partial z} = 0 \tag{1}$$

momentum equations

$$\frac{\partial u}{\partial t} + u\frac{\partial u}{\partial r} + v\frac{\partial u}{\partial z} = -\frac{1}{\rho}\frac{\partial p}{\partial r} + \nu\left(\frac{\partial^2 u}{\partial r^2} + \frac{1}{r}\frac{\partial u}{\partial r} + \frac{\partial^2 u}{\partial z^2} - \frac{u}{r^2}\right) \tag{2}$$

$$\frac{\partial v}{\partial t} + u\frac{\partial v}{\partial r} + v\frac{\partial v}{\partial z} = -\frac{1}{\rho}\frac{\partial p}{\partial z} + \nu\left(\frac{\partial^2 v}{\partial r^2} + \frac{1}{r}\frac{\partial v}{\partial r} + \frac{\partial^2 v}{\partial z^2}\right) + g\beta(T - T_f) \tag{3}$$

energy equation

$$\frac{\partial T}{\partial t} + u\frac{\partial T}{\partial r} + v\frac{\partial T}{\partial z} = \alpha\left(\frac{\partial^2 T}{\partial r^2} + \frac{1}{r}\frac{\partial T}{\partial r} + \frac{\partial^2 T}{\partial z^2}\right) \tag{4}$$

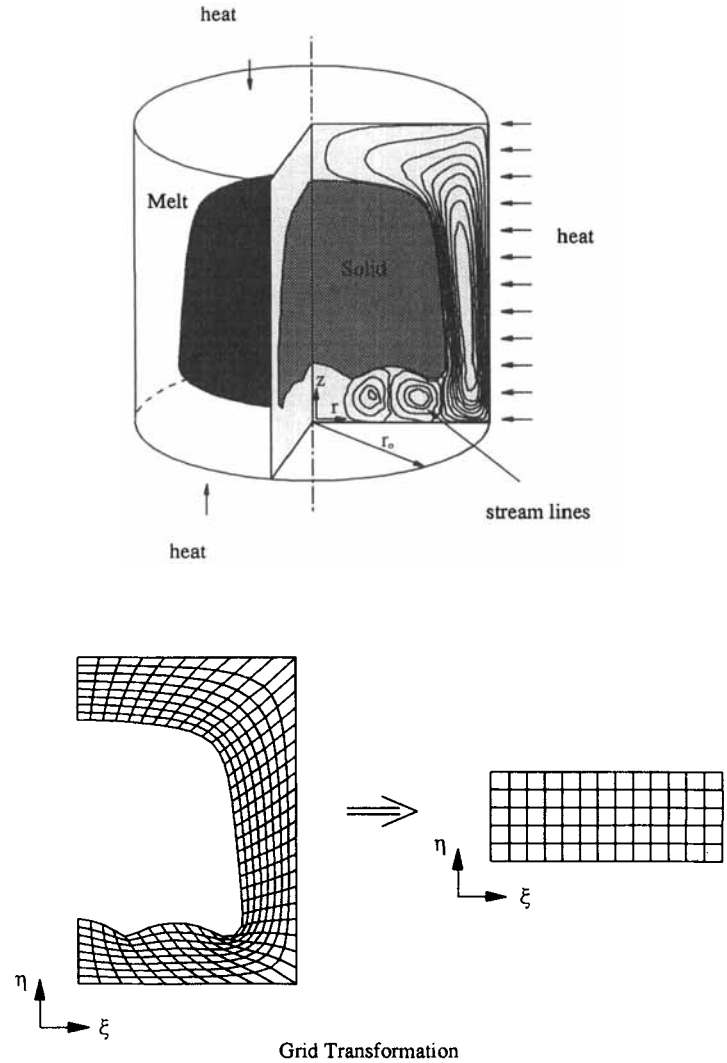

Figure 1. Schematic representation of the cylindrical capsule and grid transformation

Furthermore, since no heat conduction occurs in the solid phase, all heat transferred to the interface is utilized for melting. An energy balance for the interface yields the following condition for the moving boundary:

$$-k\frac{\partial T}{\partial n}=\rho h\frac{\partial n}{\partial t} \tag{5}$$

where n is a unit vector normal to the interface.

Introducing a length scale r_0, a time scale r_0^2/α and a temperature scale $(T_w - T_f)$, the above equations are non-dimensionalized with the following dimensionless variables:

$$R = \frac{r}{r_0}, \quad Z = \frac{z}{r_0}, \quad U = \frac{ur_0}{\alpha}$$
$$V = \frac{vr_0}{\alpha}, \quad P = \frac{p}{\alpha r_0 \rho}, \quad \theta = \frac{T - T_f}{T_w - T_f} \tag{6}$$
$$Pr = \frac{\nu}{\alpha}, \quad Ra = \frac{g\beta r_0^3 \Delta T}{\alpha \nu}, \quad \tau = Ste\, Fo = \frac{c_p \Delta T}{h} \frac{\alpha t}{r_0^2}.$$

Furthermore, since pressure is not a variable of primary interest in the present context, the momentum equations are reformulated in terms of a stream function ψ and vorticity ω defined as

$$U = \frac{1}{R}\frac{\partial \psi}{\partial Z} \tag{7}$$
$$V = -\frac{1}{R}\frac{\partial \psi}{\partial R} \tag{8}$$
$$\omega = \frac{\partial V}{\partial R} - \frac{\partial U}{\partial z} \tag{9}$$

Taking the curl of the momentum equations to eliminate pressure and using the dimensionless variables (6), the governing transport equations (1)–(5) become

vorticity

$$Ste\frac{\partial \omega}{\partial \tau} + \frac{\partial (U\omega)}{\partial R} + \frac{\partial (V\omega)}{\partial Z} = Pr\left(\nabla^2 \omega - \frac{\omega}{R}\right) + PrRa\frac{\partial \theta}{\partial R} \tag{10}$$

stream function

$$\nabla^2 \psi = \frac{2}{R}\frac{\partial \psi}{\partial R} - R\omega \tag{11}$$

energy equation

$$Ste\frac{\partial \theta}{\partial R} + U\frac{\partial \theta}{\partial R} + V\frac{\partial \theta}{\partial Z} = \nabla^2 \theta \tag{12}$$

interface energy equation

$$-\frac{\partial \theta}{\partial n} = \frac{\partial n}{\partial \tau} \tag{13}$$

TRANSFORMED EQUATIONS

As melting proceeds, the phase front moves inward while being distorted by the non-uniform heat fluxes along its surface. As a result, the shape of the solid–liquid interface will not coincide, in general, with the grid nodes of a fixed cylindrical grid. It is then difficult to implement the discretized boundary conditions and attempts to solve the resulting finite-difference equations may fail to yield accurate and convergent solutions.

To overcome these difficulties, body-fitted co-ordinates are considered. The conservation equations (10)–(13) are cast from the original cylindrical grid (R, Z) to a curvilinear grid (ξ, η) (Figure 1(b)). The resulting equations are more complicated, but their boundary conditions are now specified on straight boundaries and the computational grid is rectangular and uniformly spaced. Performing this transformation, equations (10)–(12) become in the (ξ, η) grid

$$Ste\frac{\partial\omega}{\partial\tau} + \tilde{U}\frac{\partial\omega}{\partial\xi} + \tilde{V}\frac{\partial\omega}{\partial\eta} = Pr\tilde{\nabla}^2\omega + S_\omega \tag{14}$$

$$\tilde{\nabla}^2\psi = S_\psi \tag{15}$$

$$Ste\frac{\partial\theta}{\partial\tau} + \tilde{U}\frac{\partial\theta}{\partial\xi} + \tilde{V}\frac{\partial\theta}{\partial\eta} = \tilde{\nabla}^2\theta + S_\theta \tag{16}$$

where $\tilde{U}$ and $\tilde{V}$ are contravariant velocities expressed by

$$\tilde{U} = \xi_r U + \xi_z V \tag{17}$$

$$\tilde{V} = \eta_r U + \eta_z V \tag{18}$$

and

$$\begin{aligned}
U &= \frac{1}{R}\left(\xi_z\frac{\partial\psi}{\partial\xi} + \eta_z\frac{\partial\psi}{\partial\eta}\right)\\
V &= -\frac{1}{R}\left(\xi_r\frac{\partial\psi}{\partial\xi} + \eta_r\frac{\partial\psi}{\partial\eta}\right)\\
S_\omega &= Ste\left(\xi_\tau\frac{\partial\omega}{\partial\xi} + \eta_\tau\frac{\partial\omega}{\partial\eta}\right) + \left(\frac{U}{R} - \frac{Pr}{R^2}\right)\omega + Pr\,Ra\left(\xi_r\frac{\partial\theta}{\partial\xi} + \eta_r\frac{\partial\theta}{\partial\eta}\right)\\
S_\psi &= \frac{2}{R}\left(\xi_r\frac{\partial\psi}{\partial\xi} + \eta_r\frac{\partial\psi}{\partial\eta}\right) - R\omega\\
S_\theta &= Ste\left(\xi_\tau\frac{\partial\theta}{\partial\xi} + \eta_\tau\frac{\partial\theta}{\partial\eta}\right)\\
\tilde{\nabla}^2 &= g^{11}\frac{\partial^2}{\partial\xi^2} + 2g^{12}\frac{\partial^2}{\partial\xi\partial\eta} + g^{22}\frac{\partial^2}{\partial\eta^2} + P\frac{\partial}{\partial\xi} + Q\frac{\partial}{\partial\eta} + \frac{1}{R}\left(\xi_r\frac{\partial}{\partial\xi} + \eta_r\frac{\partial}{\partial\eta}\right)
\end{aligned} \tag{19}$$

$\tilde{\nabla}^2$ is the transformed Laplacian operator in cylindrical co-ordinates.

The energy balance equation (13) for the moving interface becomes

$$\frac{\partial R}{\partial\tau} = -\frac{\partial\theta}{\partial\xi}\xi_r \tag{20}$$

$$\frac{\partial Z}{\partial\tau} = -\frac{\partial\theta}{\partial\xi}\xi_z \tag{21}$$

The boundary conditions in the computational space are:

$\xi = \xi_{\min}$ and $\xi = \xi_{\max}$

$$U = 0, \quad \frac{\partial V}{\partial\xi} = 0$$

$$\psi = 0, \quad \frac{\partial \theta}{\partial \xi} = 0$$

$$\omega = 0$$

$\eta = \eta_{\min}$

$$U = 0, \quad V = 0$$

$$\psi = 0, \quad \theta = 1$$

$$\omega = \eta_r V_\eta - \eta_z U_\eta$$

$\eta = \eta_{\max}$

$$U = 0, \quad V = 0$$

$$\psi = 0 \quad \theta = 0$$

$$\omega = \eta_r V_\eta - \eta_z U_\eta$$

The no-slip boundary condition is imposed on the surface of the enclosure and the interface. A slip boundary condition is imposed on the symmetry axis.

NUMERICAL PROCEDURE

The governing equations (14)–(16) and (20) and (21) with the corresponding boundary conditions are solved numerically with a finite-difference method. A first-order forward difference approximation is used for the time derivatives. The diffusion terms are replaced by second-order central difference approximations. Special attention is paid, however, to the convection terms. It is well known that the use of second-order central difference approximations for these terms may produce unstable and divergent solutions for high Peclet cell numbers (or high Rayleigh numbers).[10] Although the use of a first-order upwind scheme may eliminate these wiggly solutions, it introduces truncation errors and produces significant artificial diffusion. In the present study, this problem is overcome by adopting a second-order upwind scheme.

The proposed scheme has the following form:

$$u \frac{\partial f}{\partial \xi} = A^u f_{i-2} + B^u f_{i-1} + C^u f_i + D^u f_{i+1} + E^u f_{i+2} \tag{22}$$

where A^u, B^u, C^u, D^u and E^u are functions of u. These coefficients are defined in Appendix II. The resulting finite-difference scheme for the vorticity (14) and temperature equations (16) has the form

$$a_1 f_{i-2,j} + a_2 f_{i-1,j} + a_3 f_{i+1,j} + a_4 f_{i+2,j} + a_5 f_{i,j-2} + a_6 f_{i,j-1} + a_7 f_{i,j+1} + a_8 f_{i,j+2} + a_9 f_{i+1,j+1,j} + a_{10} f_{i+1,j-1} + a_{11} f_{i-1,j-1} + a_{12} f_{i-1,j+1} + a_{13} f_{i,j} = S \tag{23}$$

Expressions for the coefficients in equation (23) may be found in Reference 11. This finite-difference equation is solved by means of an alternating Penta-diagonal matrix algorithm.[11] For the stream function (equation (15)), only second-order finite differences are used and the resulting discretized equation is solved by the alternating direction implicit (ADI) procedure proposed by Roache.[10]

The overall calculation procedure consists of the following steps:

1. Set the initial values of all the variables $U_{i,j}, V_{i,j}, \omega_{i,j}$ and $\psi_{i,j}$ to zero. The initial temperatures are set to zero everywhere in the field except for the nodes at heated boundaries which are set to 1.
2. Set the initial boundary grid nodes for the physical domain.
3. Generate a new grid for the physical domain.
4. Calculate all geometric coefficients for the transformed equations.
5. Compute $\omega_{i,j}$ with the current values of $U_{i,j}$, $V_{i,j}$, $\psi_{i,j}$ and $\theta_{i,j}$.
6. Compute $\psi_{i,j}$ with the updated values $\omega_{i,j}$.
7. Compute $U_{i,j}$, $V_{i,j}$ with the updated values $\psi_{i,j}$ and velocity boundary conditions.
8. Compute $\theta_{i,j}$ with the updated values $U_{i,j}$ and $V_{i,j}$.
9. Check for convergence. If satisfied, go to the next step; otherwise, go back to step 5.
10. Check for time to stop. If positive, stop; otherwise, go to the next step.
11. Update x_0, y_0, ω_0 and θ_0 for the next time step.
12. Calculate the new interface position.
13. Perform a rezoning procedure.
14. Go back to step 3 to begin computations for the next time step.

Steps 3, 9 and 13 need further explanations. In step 3, a new grid is generated from the numerical solution of a set of two coupled non-linear elliptic partial differential equations for the cylindrical co-ordinates as a function of the curvilinear co-ordinates. This procedure is commonly used for mapping complex geometries and details concerning its implementation may be found in References 11 and 12.

In step 9, convergence is declared when

$$\sum_{i}^{N}\sum_{j}^{M} \| R \| \leqslant 10^{-4} \tag{24}$$

where $\| R \|$ is the residual for the continuity equation and when

$$\| f_{i,j}^{k+1} - f_{i,j}^{k} \| \leqslant 10^{-4} \tag{25}$$

where f denotes the vorticity and temperature and k denotes the iteration number.

According to the energy balance equation (13), the local velocity of the interface should be locally orthogonal to the interface. Generally, the melting is non-uniform along the interface because of natural convection. Therefore, the interface can become curved as the boundary is moving. If the interface becomes locally convex, the moving interface grid points have a tendency to move towards their reflex centre. As melting proceeds, the generated grids can be distorted and eventually the grid nodes may overlap. To overcome these difficulties, an implicit rezoning procedure is employed in step 13. Once the interface is determined at time level $\tau + \Delta\tau$, a spline interpolation procedure is used to redistribute the boundary grid points at equal arc length intervals along the interface. Thereby, a proper grid network system is available for carrying out the calculations at time $\tau + \Delta\tau$.

RESULTS AND DISCUSSION

The foregoing computational methodology has been thoroughly tested for natural convection dominated melting around a vertical heated cylinder[12] and within a vertical cylinder heated from below.[9] The numerical predictions were tested against other numerical solutions and experi-

mental data. These validation analyses are reported in References 9, 11 and 12 and need not be repeated here.

To avoid computational difficulties at time $\tau = 0$, a very thin uniform thickness melt layer parallel to the heated bottom, top and side walls was assumed to exist initially. The layer thickness was chosen such that the Rayleigh number based on this initial gap width was small enough so that pure conduction could be considered as the prevailing mode of heat transfer.

Following a grid refinement study and as a compromise between cost and accuracy, the calculations presented here were done with a grid size of 11×31 non-uniformly distributed nodes. This makes it possible to concentrate several grid points in the critical regions near the heated surfaces and near the solid–liquid interface where large temperature and vorticity gradients prevail. A constant time step of 10^{-3} was utilized in order to ensure small interface motion from one time step to the next. No attempts were made to optimize (increase) the time step as melting proceeds.

As a typical example, Figure 2 shows the time evolution of the streamlines and isotherms for a case with $Pr = 7{\cdot}0$, $Ste = 0{\cdot}1$, $A = 2{\cdot}0$ and $Ra = 10^5$. The increments between the streamlines and the isotherms are constant between their minimum and maximum values. At early time $\tau \leqslant 0{\cdot}01$ (Figure 2(a)), heat transfer in the melt zone is predominated by conduction, i.e. the

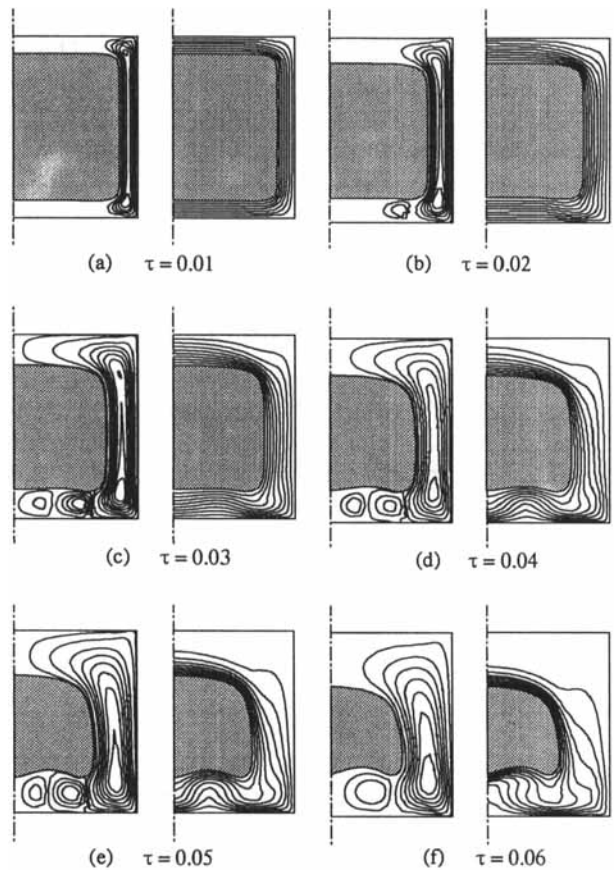

Figure 2. Time evolution of the streamlines (left) and isotherms (right) for $Ra = 10^5$

isotherms remain parallel to the heated walls, and the solid–liquid interface moves uniformly inward from the surface of the enclosure. The isotherms at the top and bottom of the cavity are horizontal and no convective flow exists. In the upper part of the capsule, heat is transferred through the melt from the top heated surface to the bottom cold melt front. As a result, layers of lighter fluid rest on layers of heavier fluid and the flow is stagnant and in a stable condition. On the other hand, at the bottom of the enclosure heat is transferred through the melt from the bottom heated surface to the top cold interface. In this case, however, the situation is potentially unstable as layers of cold and denser fluid adjacent to the solid–liquid interface lie above layers of hot and lighter fluid near the bottom heated wall. For as long as the temperature gradients remain perfectly vertical, the source term for the vorticity equation (equation (19)) is null and the flow is stagnant. In the melt layer near the vertical heated wall, a weak convective recirculating flow has already established itself. Along the vertical cylinder surface, heat is transferred to the melt and the fluid moves upward. Along the vertical phase front, heat is transferred to the interface and the fluid descends. At $\tau = 0{\cdot}02$ (Figure 2(b)), the melt layer around the solid phase is thicker and the unstable thermal situation at the bottom of the enclosure leads to a Bénard clockwise recirculating cell. Due to the long counterclockwise recirculation bubble along the side of the cylinder, it is observed that the onset of Bénard convection occurs at a much earlier time than that for the case of bottom heating only.[9] At $\tau = 0{\cdot}03$ (Figure 2(c)), a second Bénard counterrotating cell has appeared in the bottom layer. As melting proceeds, the Bénard cell at the right, entrained by the lateral counterclockwise recirculation bubble, grows faster and stronger than the left one (Figure 2(d)–2(e)). As a result, the left cell is pushed leftward and shrinks until it vanishes completely (Figure 2(f)).

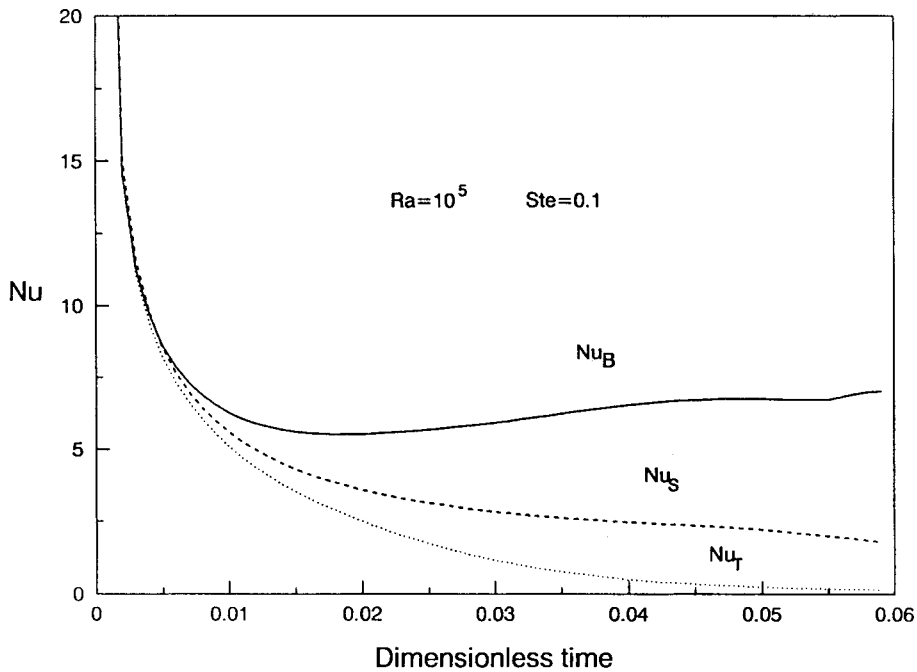

Figure 3. Timewise variation of the average Nusselt numbers at the bottom (Nu_B), at the vertical (Nu_S) and at the top (Nu_T) surface for $Ra = 10^5$

The timewise variations of the average Nusselt number at the bottom (Nu_B), at the side (Nu_S) and at the top (Nu_T) of the cylinder are depicted in Figure 3. These Nusselt numbers were calculated from the converged temperature field at each time step. The results display a rapid decrease in the heat transfer rate at the early stages of melting which is indicative of transient heat conduction. As soon as natural convection sets in the lower part of the enclosure with the appearance of Bénard cells ($\tau \leqslant 0{\cdot}02$), the heat transfer rate, i.e. Nu_B, starts increasing. As time passes, the melt layer between the vertical cylinder surface and the vertical phase front expands and the thermal resistance across this layer increases. This results in a constant decrease in the magnitude of Nu_S. On the other hand, it is seen that the Nusselt number at the top, Nu_T, decreases monotonically to zero. This is the result of the gradual decrease of the temperature gradients in the upper region of the capsule generated by the continuous upward flow along the vertical heated surface. As the phase front moves away from the top heated surface, the melt region at the top of the cylinder becomes an isothermal zone as shown by the isotherms in Figure 2(f).

Figure 4 shows the time evolution of the streamlines and isotherms for $Ra = 10^6$ with the other parameters remaining unchanged. Due to the stronger convective motion inside the melt layer along the vertical heated wall, Bénard convection appears much earlier ($\tau < 0{\cdot}004$). The momentum of the clockwise recirculating Bénard cell at the right is large enough to create and

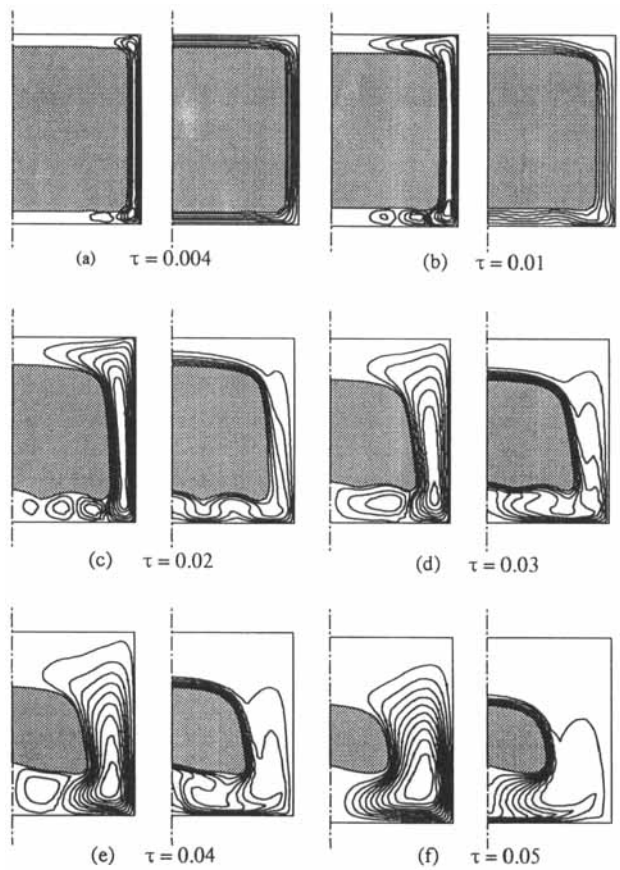

Figure 4. Time evolution of the streamlines (left) and isotherms (right) for $Ra = 10^6$

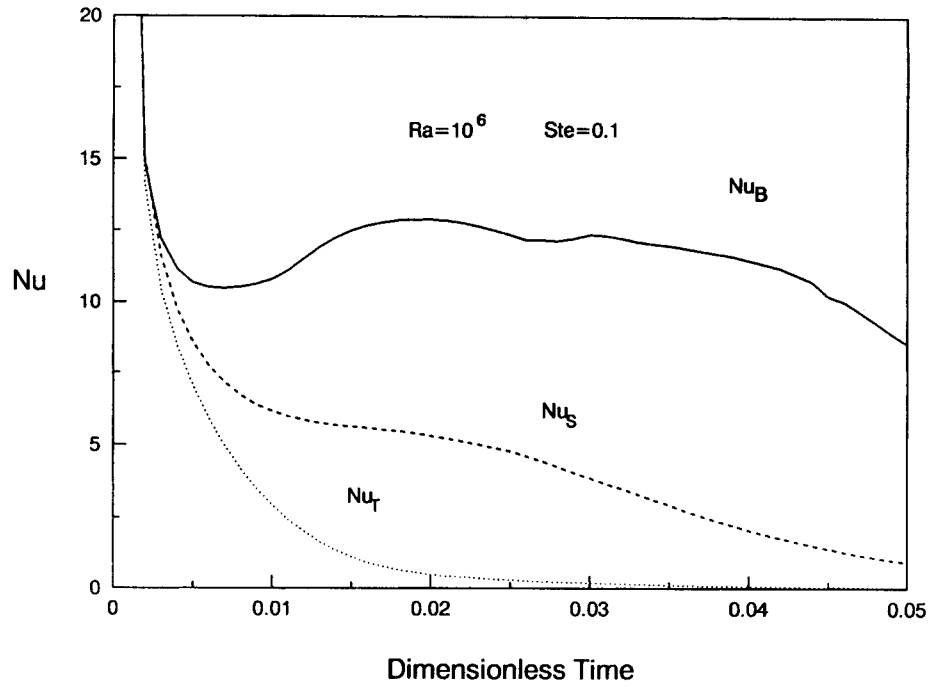

Figure 5. Timewise variation of the average Nusselt numbers at the bottom (Nu_B), at the vertical (Nu_S) and at the top (Nu_T) surface for $Ra = 10^6$

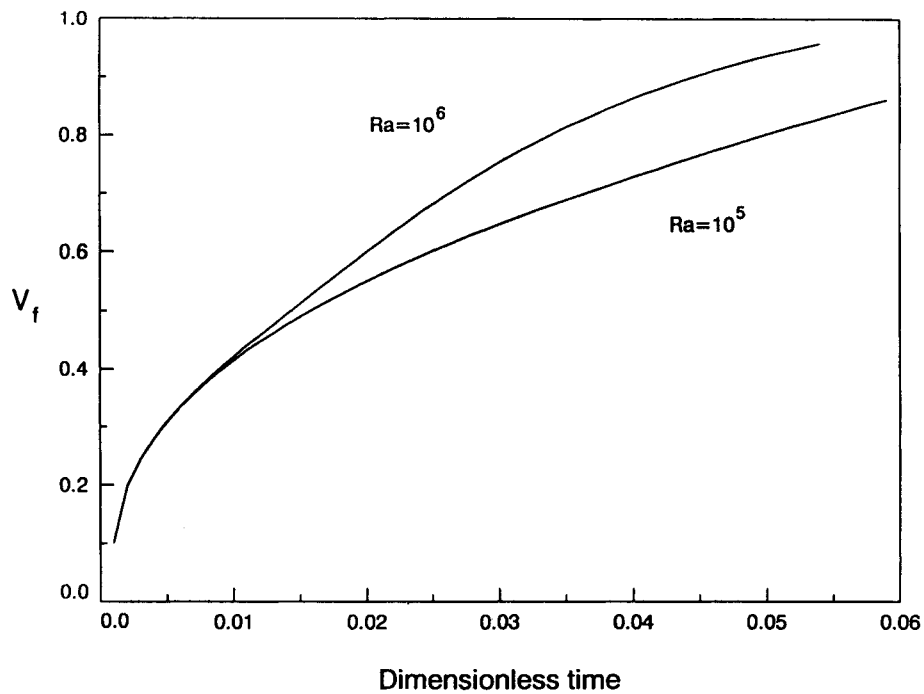

Figure 6. Temporal variation of the molten volume fraction

entrain two additional cells (Figure 4(c)). As a result, the isotherms are considerably perturbed and so are the heat transfer rates and the time evolution of the phase front at the bottom of the cylinder. Once again, as melting proceeds, the melt layer at the bottom expands and the Bénard cell at the right grows faster and stronger than the left ones. The left cells are pushed leftward and shrink until they vanish (Figure 4(d)). The remaining clockwise recirculating cell at the bottom then starts decreasing as the lateral counterclockwise recirculating cell grows in size (Figure 4(e)). Eventually the latter engulfs the former (Figure 4(f)).

Figure 5 illustrates the corresponding timewise variation of the average Nusselt numbers. Due to the more intense convective motion, the monotonic decrease of Nu_T is faster than that for the previous case. The onset and the development of Bénard convective cells is clearly seen as Nu_B increases from $\tau = 0{\cdot}01$ to $\tau = 0{\cdot}02$. For $\tau \geqslant 0{\cdot}02$, these cells merge to become one and Nu_B starts decreasing again. The qualitative behaviour of Nu_S is the same as for the previous case.

The temporal variation of the molten volume fraction was also determined from a numerical integration of the melt cavity volume and is shown in Figure 6. It is seen that this fraction increases almost linearly with time once the convective motion is well established throughout the melt.

CONCLUDING REMARKS

A numerical study of natural convection dominated melting within an isothermal vertical cylinder has been conducted. A robust computational methodology based on body-fitted co-ordinates was adopted for handling the complex motion and irregular shape of the time-varying solid–liquid interface. Results have shown that heat transfer for the top heated surface is predominated by conduction. The Nusselt number at the top surface decreases monotonically to zero as melting progresses, showing that no heat is transferred across the top layer once natural convection is fully developed in the melt. The highest heat transfer rates are observed for the bottom surface with the onset and development of Bénard convective cells. Due to the convective motion of the flow along the vertical heated wall, the onset of Bénard convection occurs at a much earlier time than that for the case of melting within a cylinder heated from below.

ACKNOWLEDGEMENTS

The authors are very grateful to the National Science and Engineering Research Council of Canada for their financial support. They also thank Miss Plante for typing this manuscript.

APPENDIX I

Nomenclature

A	aspect ratio (H/r_0)
c_p	specific heat
Fo	Fourier number $(\alpha t/r_0^2)$
g	acceleration of gravity
g^{11}	$\xi_r^2 + \xi_z^2$
g^{12}	$\xi_r\eta_r + \xi_z\eta_z$
g^{22}	$\eta_r^2 + \eta_z^2$

h latent heat of fusion
H height of cylinder
J^{-1} $\xi_r\eta_z - \xi_z\eta_r$
k thermal conductivity of PCM
n unit vector
M number of nodes (axial direction)
N number of nodes (radial direction)
Nu Nusselt number $(q/(Hk(T_w - T_f)))$
p pressure
P forcing function in grid generation
PCM phase change material
Pr Prandtl number ν/α
q heat transfer rate
Q forcing function in grid generation
r radial co-ordinate
r_0 radius of the cylinder
R dimensionless radius (r/r_0)
Ra Rayleigh number $(g\beta r_0^3(T_w - T_f)/\alpha\nu)$
Ste Stefan number $(c_p(T_w - T_f)/h)$
t time
T temperature
u, v radial and axial velocities
U, V dimensionless velocities $(ur_0/\alpha, vr_0/\alpha)$
$\tilde{U}, \tilde{V}$ contravariant velocities
V_f molten volume fraction
z axial co-ordinate
Z dimensionless axial co-ordinate (z/r_0)

Greek letters

α thermal diffusivity
β thermal expansion coefficient
ξ, η co-ordinates in transformed plane
ξ_r r_η/J
ξ_z $-r_\eta/J$
η_r $-z_\xi/J$
η_z r_ξ/J
ξ_τ $\xi_r r_\tau + \xi_z z_\tau$
η_τ $\eta_r r_\tau + \eta_z z_\tau$
θ dimensionless temperature $((T - T_f)/(T_w - T_f))$
ν kinematic viscosity
τ dimensionless time $(Ste\,Fo)$
ψ stream function
ω vorticity $(\partial V/\partial R - \partial U/\partial Z)$
∇^2 Laplacian in cylindrical co-ordinates
$\tilde{\nabla}^2$ transformed Laplacian

Subscripts

f fusion
w cylinder wall

APPENDIX II

Coefficients in equation (22) are

$$A^u = \frac{|u| + u}{4\Delta\xi}$$

$$B^u = -\frac{|u| + u}{\Delta\xi}$$

$$C^u = \frac{3|u|}{2\Delta\xi}$$

$$D^u = -\frac{|u| - u}{\Delta\xi}$$

$$E^u = \frac{|u| - u}{4\Delta\xi}$$

REFERENCES

1. T. Saitoh and K. Hirose, 'High Rayleigh number solutions to problems of latent heat thermal energy storage in a horizontal cylinder capsule', *J. Heat Transfer*, **104,** 545–553 (1982).
2. H. Rieger, U. Projahn, M. Bareiss and H. Beer, 'Heat transfer during melting inside a horizontal tube', *J. Heat Transfer*, **105,** 226–234 (1983).
3. C. J. Ho and R. Viskanta, 'Heat transfer during inward melting in a horizontal tube'. *Int. J. Heat Mass Transfer*, **27,** 705–716 (1984).
4. M. Bareiss and H. Beer, 'An analytical solution of the heat transfer process during melting of an unfixed solid phase change material inside a horizontal tube', *Int. J. Heat Mass Transfer*, **27,** 739–746 (1984).
5. A. Prasad and S. Sengupta, 'Numerical investigation of melting inside a horizontal cylinder including the effects of natural convection', *J. Heat Transfer*, **109,** 803–806 (1987).
6. A. Prasad and S. Sengupta, 'Nusselt number and melt time correlations for melting inside a horizontal cylinder subjected to an isothermal wall temperature condition', *J. Solar Energy Eng.*, **110,** 340–345 (1988).
7. C. J. Ho and K. C. Liu, 'Outward melting in a cylindrical annulus', *J. Energy Resources Technol.*, **108,** 240–244 (1986).
8. E. M. Sparrow and J. A. Broadbent, 'Inward melting in a vertical tube which allows free expansion of the phase-change medium', *J. Heat Transfer*, **104,** 309–315 (1982).
9. M. Prud'Homme, T. H. Nguyen, and Y. K. Wu, 'Simulation numérique de la fusion à l'intérieur d'un cylindre adiabatique chauffé par le bas', *Int. J. Heat Mass Transfer*, **34,** 2275–2286 (1991).
10. P. J. Roache, *Computational Fluid Dynamics*, Hermosa Publishers, Albuquerque, New Mexico, 1976.
11. Y. K. Wu, 'Numerical studies of melting process in a cylindrical enclosure', *Ph.D. Thesis*, École Polytechnique de Montréal, 1990.
12. Y. K. Wu, M. Prud'Homme and T. H. Nguyen, 'Étude numérique de la fusion autour d'un cylindre verticals soumis à deux types de conditions limites', *Int. J. Heat Mass Transfer*, **32,** 1927–1938 (1989).